Korean J. Chem. Eng., 39(12), 3377-3388 (2022)
DOI: 10.1007/s11814-022-1181-5

pISSN: 0256-1115
eISSN: 1975-7220

Construction of g/C_3N_4-ZnO composites with enhanced visible-light photocatalytic activity for degradation of amoxicillin

Shuhan Sun*, Shiling Li*, Yibing Hao*, Xiao Yang, and Xiaomin Dou*,***,†**

*Beijing Key Lab for Source Control Technology of Water Pollution, College of Environmental Science and Engineering, Beijing Forestry University, Beijing 100083, China
**Key Laboratory of Land Surface Pattern and Simulation, Institute of Geographic Sciences and Natural Resources Research, Chinese Academy of Sciences, Beijing 100101, China
***Engineering Research Center for Water Pollution Source Control & Eco-remediation, Beijing Forestry University, Beijing 100083, China

(*Received 15 March 2022 • Revised 14 May 2022 • Accepted 18 May 2022*)

Abstract−g/C_3N_4-ZnO composite catalysts were synthesized through surface hybridization of the delocalized conjugated-π structure of g/C_3N_4 with the closely contacted surface of ZnO *via* a successive and simultaneous calcination procedure, and two kinds of photocatalysts, g/C_3N_4-ZnO1 and g/C_3N_4-ZnO2, were obtained. Heterojunctions were formed between the two components, which promote the separation of photogenerated carriers efficiently, and then enhanced the degradation of 100 mg/L of AMX. The degradation rate of g/C_3N_4-ZnO1 was 1.54, 11.33, and 2.52-fold that of g/C_3N_4-ZnO2, g/C_3N_4, and ZnO, respectively, at a 3.5-h reaction period, with the dosage of 0.3 g/L, and solution pH at 7.0±0.2. The recycle and reuse ability was excellent and 90.5% of AMX mitigation was achieved in the fifth cycle. For g/C_3N_4-ZnO1, electrons migrated from the conduction band of g/C_3N_4 to that of ZnO *via* the heterojunction. ·OH and h^+ were the main active species for AMX degradation, compared to $\cdot O_2^-$ dominated for g/C_3N_4. Twelve intermediate products were identified, and two degradation pathways were inferred for g/C_3N_4-ZnO1 and g/C_3N_4-ZnO2, respectively. Finally, transformation products without lactam rings were achieved, which lost most of the antibacterial potencies, and the ecotoxicity was also dramatically decreased as indicated by the ECOSAR program.

Keywords: Amoxicillin, Antibiotics, g/C_3N_4, Catalyst, Photocatalysis

INTRODUCTION

Antibiotic production wastewater (APW) discharged from pharmaceutical industries usually contains high concentrations of antibiotic residues that are toxic and inhibitive to bacteria in biological treatment units, and are also hazardous and harmful to habits of receiving water body if not well processed and managed. β-lactam antibiotics, targeted at penicillin-binding proteins of bacteria to inhibit cell biosynthesis, are reported to account for over 65% of the antibiotic consumption [1]. Amoxicillin (AMX) is one of the most widely used β-lactam ring antibiotics used both for humans and animals. The occurrence and concentration of AMX in antibiotic production wastewater is in the range of 20-200 mg/L [2]. Anaerobic digestion and thermal hydrolytic treatment have been employed for AMX mitigation. The bacterial activity in anaerobic units was inhibited by high concentrations of AMX, often accompanied by a prolonged hydraulic retention time. In addition, concerns were raised from bacteria resistance gene proliferation and spreading in anaerobic units. Thermal hydrolysis of AMX was effective but was subjected to the high specific heat capacity of water (4,182 J/kg.°C) and high energy input for general convection-diffusion-based heating. Advanced oxidation processes (AOPs) against AMX have been developed and applied extensively for antibiotic pretreatment and have proven to be effective.

Visible-light-driven photodegradation in AOP methods is attractive for antibiotic deactivation due to its high efficiency, green energy sources, and eco-friendly nature. As an n-type semiconductor of two-dimensional layered π-conjugated polymer, graphitic carbon nitride (g/C_3N_4) is metal-free, non-toxic, environmentally friendly, low cost, and has a relatively narrow bandgap (2.70 eV) and high physical and chemical stability [3]. High visible light absorption due to its narrow bandgap and appealing electronic band structure makes it one of the most promising catalysts for AMX photodegradation [4]. However, the small specific surface area, rapid recombination of electron-hole pairs, and low carrier mobility restrict its catalytic performance [5]. Diversified ways, including nanoarchitecture designing, functionalization, and modification, have been tried to construct novel g/C_3N_4 and g/C_3N_4-based composites with tuned band structures and preferred heterojunctions and enhanced photocatalytic activities accordingly [6]. Introducing another semiconductor as a cocatalyst is a facile way to form multicomponent heterojunction for g/C_3N_4 modification [7]. ZnO, as a suitable candidate, is promising due to its remarkable properties, such as inexpensive, abundant reserves, ecologically sound, good biocompatibility, easy-to-prepare, and physicochemical/thermal stability [8]. Enhanced photocatalytic activity of g/C_3N_4-ZnO composite was achieved through

†To whom correspondence should be addressed.
E-mail: douxiaomin@bjfu.edu.cn
Copyright by The Korean Institute of Chemical Engineers.

surface hybridization of the delocalized conjugated-π structure of g/C_3N_4 with closely contacted surfaces of ZnO to reduce the dangling bonds of ZnO [9]. Varied amounts of g/C_3N_4 (1-80%) were introduced to the surfaces of ZnO, and enhanced photocatalysis performance was achieved for pollutant degradation, H_2 evolution, and CO_2 reduction [10,11]. Good dispersion of ZnO on g/C_3N_4 or *vice versa* is critically important to constructing heterojunctions or wrapping structures. Loading a very small amount of ZnO (<1%) on g/C_3N_4 is expected to enhance the dispersibility, generate abundant contacting interfaces between the two components, and achieve unexpected benefits.

In this work, a small amount of ZnO (<0.25%) was decorated on g/C_3N_4 under a successive and simultaneous calcination procedure, respectively, to prepare composite photocatalysts towards AMX degradation under visible light exposure. The main objectives were (1) to evaluate the interactive effects of loading a small amount of ZnO and the calcination procedures, and (2) to understand the differences in performances and degradation mechanisms of AMX by the two kinds of photocatalysts yielded through different calcination procedures.

MATERIALS AND METHODS

1. Chemicals and Materials

Hydrochloric acid (36-38%), sodium hydroxide (98%), urea (99%), zinc acetate (99%), P-benzoquinone (99%), EDTA-2Na (≥99.0%), silver nitrate are analytical grade and used without further purification. The chromatographic reagents mainly included methanol (≥99.9%), acetonitrile (≥99.9%), isopropanol (≥99.7%), potassium dihydrogen phosphate (≥99.5%). AMX (≥98%) was purchased from Shanghai Aladdin Biochemical Technology Co., Ltd. Deionized water was used for all experiments.

2. Materials Synthesis

Urea and zinc acetate as the precursors, under a successive and simultaneous calcination procedure, were used to synthesize g/C_3N_4-ZnO photocatalysts, respectively. (1) g/C_3N_4-ZnO1. 10 g of urea and a certain amount of ZnO were mixed by thoroughly grinding and transferred to a covered crucible in a muffle furnace. The temperature was raised from ca. 20 °C to 550 °C at 10 °C/min and kept for 3 h. When cooled to room temperature naturally, the material was collected for further use and named g/C_3N_4-ZnO1. (2) g/C_3N_4-ZnO2. The precursors were prepared following similar procedures as that for g/C_3N_4-ZnO1 and transferred to a muffle furnace. The temperature was raised to 300 °C at 10 °C/min and held for 2 h, and then increased up to 500 °C at 5 °C/min and kept for 1 h. When cooled to room temperature naturally, the material was collected and named g/C_3N_4-ZnO2. For comparison, pure g/C_3N_4 and pure ZnO were separately synthesized using a similar process. The yields were 6.5 g, 7.0 g and 7.0 g for g/C_3N_4, g/C_3N_4-ZnO1 and g/C_3N_4-ZnO2, respectively, in each calcination process.

3. Catalyst Characterization

The microstructure of the synthesized catalysts was observed by a Titan3^{TM} G2 60-300 double aberration-corrected spectrometer (FEI, USA). The X-ray diffraction (XRD) patterns of the samples were collected on an XRD-7000 diffractometer (Shimadzu, Japan) using a Cu Kα radiation source. The chemical components and valence states of the catalysts were analyzed on an ESCALAB 250 X-ray photoelectron spectrometer (XPS) (Thermo Scientific, USA) with Al Kα radiation as the excitation source. Fourier transform infrared spectra (FTIR) were recorded at room temperature on a Vertex 70 FTIR spectrometer (Bruker, Germany) at a 2 cm^{-1} resolution. The photoluminescence (PL) emission spectra were measured by a FluoroMax®-4 spectrofluorometer (HORIBA, Japan). The photocurrent was obtained on CHI 660E electrochemical workstation (Chenhua Instruments, China) equipped with a standard three-electrode system. A Pt foil electrode was the counter electrode and an Ag/AgCl electrode was the reference electrode. The UV-vis spectra were measured by a UV2450 UV-vis spectrometer (Shimadzu, Japan) using $BaSO_4$ as a reference. The specific surface area was analyzed by a BELSORP Minix surface area analyzer (Microtrac, USA) through nitrogen adsorption-desorption at 77 K.

4. Photocatalytic Performance

AMX degradation experiments were carried out in a PCX 50B multi-channel photocatalytic reactor (Perfectlight, China). In each test, 40 mL of 100 mg/L AMX aqueous solution was employed and the catalyst dosage was 0.3 g/L. Initially, the mixture was magnetically stirred in dark for 0.5 h to reach an adsorption-desorption equilibrium. Under visible light irradiation, 0.5 mL of suspension was collected at predetermined time intervals and filtered through 0.22-μm Millipore filters to remove the catalysts, and then stored at −20 °C and analyzed within 36 h. The concentration of AMX was determined on high-performance liquid chromatography (HPLC) equipped with a UV detector at 30 °C. The detection wavelength of the UV detector was 240 nm and the injection volume was 10 μL. The isocratic mobile phase consisted of 70% potassium dihydrogen phosphate (0.025 mol/L) and 30% acetonitrile and was run at a flow rate of 0.6 mL/min. The transformation products of AMX were separated on an Ultimate 3000 ultrahigh-performance liquid chromatograph (Dionex, USA) and detected using a microTOF Q II time-of-flight mass spectrometer (Bruker, Germany). To estimate the photostability of the photocatalysts, the solid samples were recycled after each photocatalytic test and reused in the subsequent test.

5. Active Species Analysis

The main active species and their roles in photocatalytic degradation of AMX were evaluated by adding 0.05 mmol/L of isopropanol (IPA), benzoquinone (BQ), ethylenediaminetetraacetic acid disodium salt (EDTA-2Na), and silver nitrate ($AgNO_3$) to scavenge hydroxyl radicals (·OH), superoxide radical ($\cdot O_2^-$), holes (h^+) and electrons (e^-), respectively [12]. Additionally, a nitroblue tetrazolium (NBT) method was used to quantify the amounts of $\cdot O_2^-$ [13]. The photocatalysts (12 mg) were added into 40 mL of 5×10^{-5} mol/L NBT solution, shaken at 250 rpm in dark for 30 min before irradiation. The suspensions were irradiated and sampled at 5, 10, 15, 20, 25, 30 min, respectively, and then filtrated. The samples were analyzed on a 756 PC UV-vis spectrophotometer at 259 nm.

6. Electrochemical Determination Method

The electrochemical properties of the catalysts were measured using a CHI 660E electrochemical workstation (Chenhua Instruments, China) assembled with a standard three-electrode system. Pt was used as the counter electrode, and Ag/AgCl was used as reference electrode. A visible light source with the same wavelength range as that used for catalysis was employed, and 0.5 mol/L Na_2-

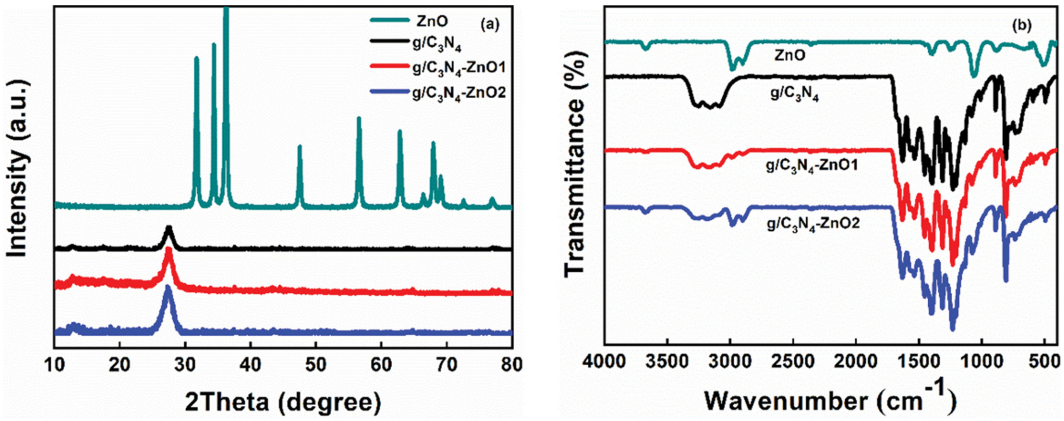


Fig. 1. (a) XRD patterns and (b) FTIR spectra of ZnO, g/C_3N_4, g/C_3N_4-ZnO1 and g/C_3N_4-ZnO2.

SO_4 was used as electrolyte solution. The working electrode was prepared following a procedure: (1) mixing 10 mg of catalyst material with 1 mL of ethanol in a covered glass bottle, (2) ultrasonic treating the mixture for 1 h, (3) using a pipette to transfer 100 μL of suspension to the FTO glass electrode, and (4) moving the electrode coated with photocatalysts to the oven, and drying it at 180 °C for 1 h, and used for measurement. The excitation wavelength of the PL spectrum is 310 nm.

RESULTS AND DISCUSSION

1. Characterization of As-prepared Photocatalyst

The TEM image of g/C_3N_4 (Fig. S1) shows a typical multilayer structure of graphite carbonitride, which corresponds to in-plane stacking of triazine units revealed by XRD patterns. ZnO and g/C_3N_4 present granular and flake shapes, respectively. The surface of g/C_3N_4-ZnO composites presents highly porous, smooth, thin, and flat-layered features. The plane-layered morphology is due to the spalling of the two-dimensional structure of graphite carbonitride. In the synthesis process, urea releases a large amount of CO_2, H_2O, NH_3, and other gases. These gases made the surface of graphite carbonitride porous and weakened the van der Waals force between the intermediate layers of conjugated aromatic motifs in the triazine system [14]. Agglomerated fine nanoparticles were dispersed on the flat structure of graphite carbonitride in TEM images. The tiny nanoparticles bound on the surfaces of g/C_3N_4 were identified as ZnO, which was from zinc acetate after calcination. The O to Zn ratio was 1 : 1 as revealed by EDX.

The XRD patterns of ZnO, g/C_3N_4, g/C_3N_4-ZnO1, and g/C_3N_4-ZnO2 are provided in Fig. 1(a). Two peaks at 27.4° and 12.9° are observed for g/C_3N_4, assigned to interlayer stacking of the conjugated aromatic rings and in-plane stacking of triazine units (JCPDS 87-1526), respectively [15]. The diffraction peaks (ca. 34.4°, 36.1°, and 56.7°) of ZnO can be exactly indexed as the hexagonal wurtzite phase (JCPDS 36-1451) [16]. The XRD patterns of g/C_3N_4-ZnO1 and g/C_3N_4-ZnO2 are similar to each other and to that of g/C_3N_4. No characteristic peaks were observed for ZnO due to its low content (e.g., 5 mg ZnO in 10 g of g/C_3N_4) in the composites.

The FTIR spectra of the four samples are presented in Fig. 1(b). Four groups of characteristic IR bands at ca. 491, 1,382, 2,997-2,998, and 3,677 cm^{-1}, appeared for ZnO, which were assigned to the stretching vibration of Zn-O, chemical binding of oxygen in the C=O group on the surface of ZnO, stretching vibration of C-H from an alkane, and stretching vibration of O-H, respectively. The three samples, g/C_3N_4, g/C_3N_4-ZnO1, and g/C_3N_4-ZnO2, showed very similar IR patterns. The bands at 811, 1,200-1,700, and 3,000-3,500 cm^{-1} were from the typical breathing mode of tri-s-triazine units, the C-N stretching vibration, and the stretching vibration of N-H, respectively [8]. No representative IR bands of ZnO appeared in both g/C_3N_4-ZnO1 and g/C_3N_4-ZnO2 due to a low loading weight.

The XPS full survey and narrow scans of the samples are presented in Fig. 2. The C1s spectra (Fig. 2(b)) present one strong peak at 288.0 eV and two weak peaks at 284.7 eV and 293.7 eV, assigned to N=C-N, C=C, and π excitation, respectively [17]. The N1s peaks centered at ca. 398.4 eV are related to C=N-C/N-Zn (Fig. 2(c)) [18]. Two peaks at 1,021.9 eV and 1,045.1 eV, are due to Zn $2p_{3/2}$ and Zn $2p_{5/2}$, respectively (Fig. 2(d)) [19]. The O1s peak at 530.31 eV is from Zn-O, and the peak at 531.70 eV is from the -OH group and H_2O. The C1s and N1s spectra both positively shifted by 0.48 and 0.46 eV, 0.44 and 0.40 eV for g/C_3N_4-ZnO1 and g/C_3N_4-ZnO2, compared to that of g/C_3N_4, indicating N-Zn bonds formed between g/C_3N_4 and ZnO [20].

All catalysts presented type IV isotherms with type H3 hysteresis loops according to the IUPAC classification (Fig. S2). The specific surface areas are 142.1, 144.6, and 168.7 m^3/g for g/C_3N_4, g/C_3N_4-ZnO1, and g/C_3N_4-ZnO2, respectively, while pore sizes span from micro-, meso- to macro-scale, ranging from 2 nm to 150 nm (Table 1). After doping of ZnO, the surface area increases, while the pore size narrows down, which may be caused by the accumulation of nanosized ZnO in the voids of 2D layers of g/C_3N_4.

Table 1. Porosity characteristics of g/C_3N_4, g/C_3N_4-ZnO1, and g/C_3N_4-ZnO2

Photocatalyst	Specific surface area (m^2/g)	Pore volume (cm^3/g)	Pore diameter (nm)
g/C_3N_4	142.073	0.643	3.071
g/C_3N_4-ZnO1	144.571	0.740	20.620
g/C_3N_4-ZnO2	168.691	0.618	16.763

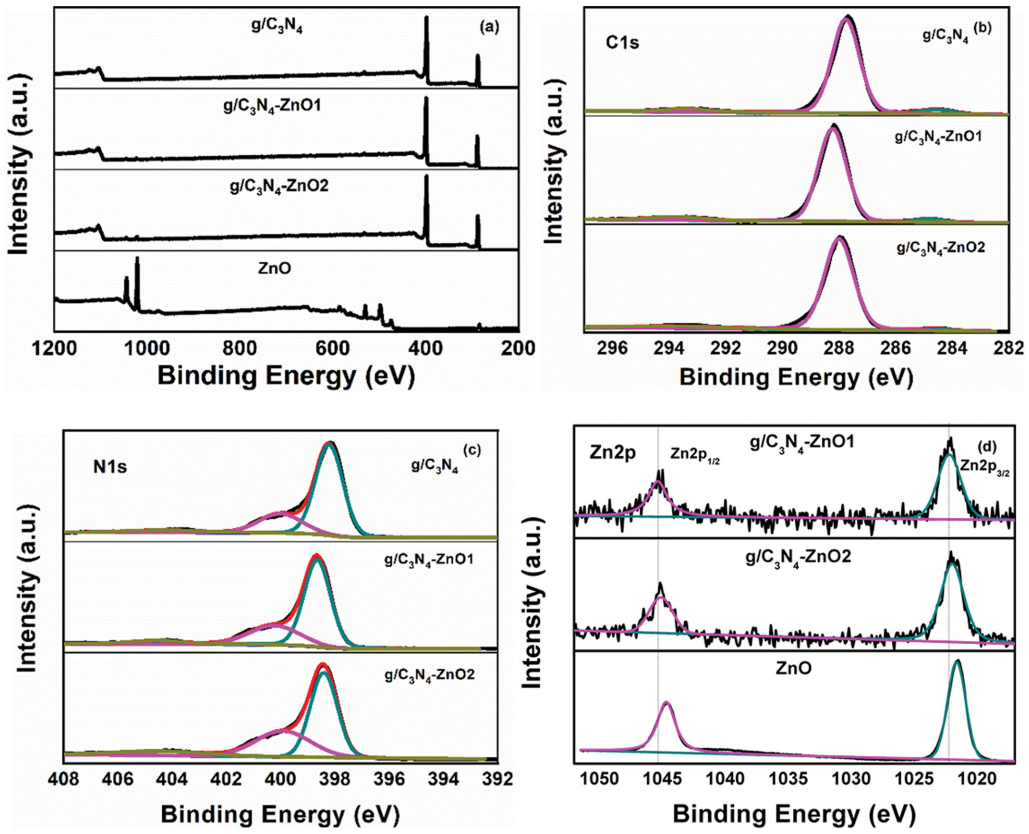


Fig. 2. (a) Full scan, (b) C1s, (c) N1s and (d) Zn2p XPS spectra of g/C_3N_4, ZnO, g/C_3N_4-ZnO1 and g/C_3N_4-ZnO2.

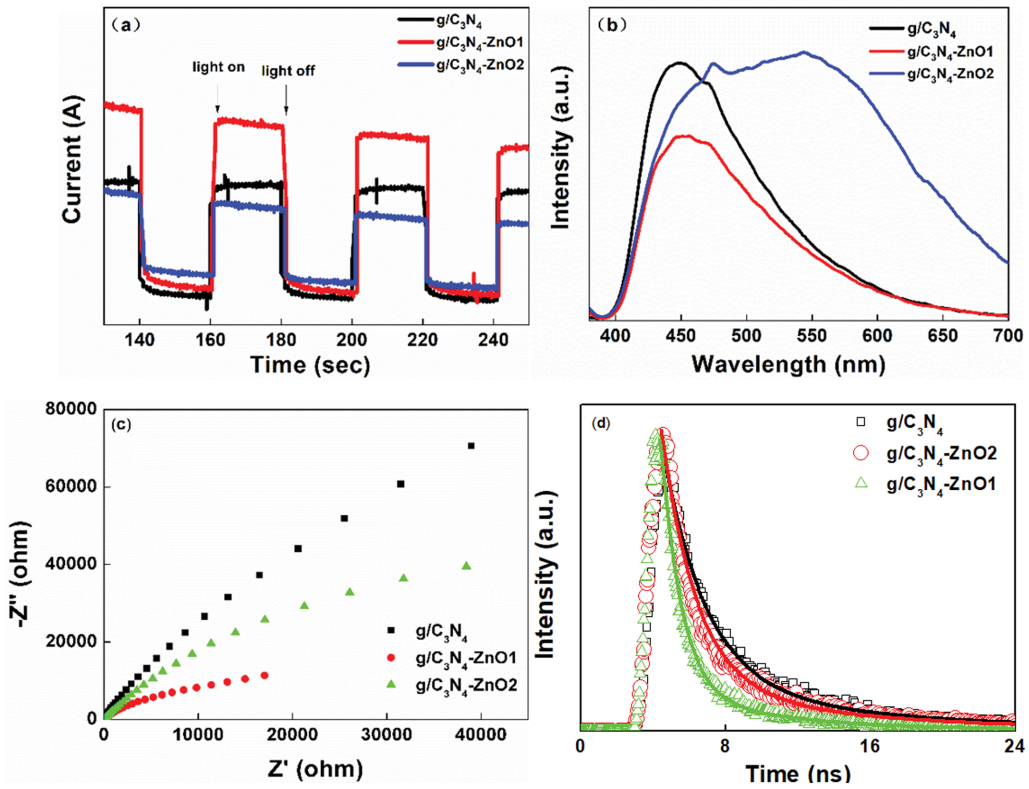


Fig. 3. (a) Transient photocurrent responses, (b) photoluminescence (PL) spectra, (c) electrochemical impedance spectroscopy (EIS) and (d) time resolved fluorescence spectra (TR-PL) of g/C_3N_4, g/C_3N_4-ZnO1, and g/C_3N_4-ZnO2.

2. Photochemical Properties of Catalysts

The transient photocurrent response, fluorescence spectra, electrochemical impedance spectroscopy and time resolved fluorescence spectroscopy of g/C_3N_4, g/C_3N_4-ZnO1, and g/C_3N_4-ZnO2 are provided in Fig. 3. In an AM1.5G irradiation (Standard Test Conditions, STC, 100 mW/cm^2) cycle, all catalysts show sensitive photocurrent response following the order of g/C_3N_4-ZnO1>g/C_3N_4>g/C_3N_4-ZnO2 (Fig. 3(a)). This result demonstrates that strong electronic interaction between g/C_3N_4 and ZnO in g/C_3N_4-ZnO1 can effectively improve charge migration efficiency and it is obvious that g/C_3N_4 and ZnO phases in g/C_3N_4-ZnO1 were well combined as expected and promoted light absorption. The decreased photocurrent for g/C_3N_4-ZnO2 indicated that not all the combinations of g/C_3N_4 and ZnO can effectively improve the light absorption, promote the carrier transmission and strengthen the photocurrent response [21]. g/C_3N_4-ZnO1 can realize the effective combination of g/C_3N_4 and ZnO.

As shown in Fig. 3(b), the PL peak intensity of g/C_3N_4 is the highest, which indicates that the semiconductor has a high recombination efficiency. After loading of ZnO, the PL intensity of g/C_3N_4-ZnO1 decreased remarkably, due to the effective separation of photoexcited electrons and holes. The PL profile of g/C_3N_4-ZnO2 is in a broad range and is similar to that of g/C_3N_4, which indicates the separation of electrons and hole is not as effective as that of g/C_3N_4-ZnO1 under irradiation. The electrochemical impedance spectroscopy (EIS) of g/C_3N_4, g/C_3N_4-ZnO1, and g/C_3N_4-ZnO2 are presented in Fig. 3(c). The smaller the radius of the semicircle was overserved, the smaller the impedance was, which indicated the higher separation degree of photogenerated carriers [22]. The sizes of the radii follow the order of g/C_3N_4>g/C_3N_4-ZnO2>g/C_3N_4-ZnO1, which confirms that the impedance of g/C_3N_4-ZnO1 is the smallest and the separation and mobility efficiency of carriers was the highest. As shown in Fig. 3(d) and Table 2, the average carrier lifetimes of g/C_3N_4, g/C_3N_4-ZnO1 and g/C_3N_4-ZnO2 are 8.72, 5.11 and 7.76 ns, respectively. The average life of carriers in g/C_3N_4-ZnO1 and g/C_3N_4-ZnO2 are 0.59 and 0.89 times of that in g/C_3N_4, respectively, indicating that g/C_3N_4-ZnO1 and g/C_3N_4-ZnO2 have relatively high carrier transmission capacity and relatively fast transmission speed in compassion with g/C_3N_4.

Table 2. Fluorescence decay lifetimes and related parameters of photo-excited charge carriers for g/C_3N_4, g/C_3N_4-ZnO1 and g/C_3N_4-ZnO2

Photocatalysts	i	f_i (%)	t_i (ns)	t_{ave} (ns)
g/C_3N_4	1	58.87	2.32	8.72
	2	41.13	10.71	
g/C_3N_4-ZnO1	1	65.06	1.09	5.11
	2	34.94	6.39	
g/C_3N_4-ZnO2	1	61.69	1.88	7.76
	2	38.31	9.61	

3. Photocatalytic Performance

The photodegradation of AMX against time using g/C_3N_4-ZnO1 and g/C_3N_4-ZnO2 is presented in Fig. 4. In addition, the structure

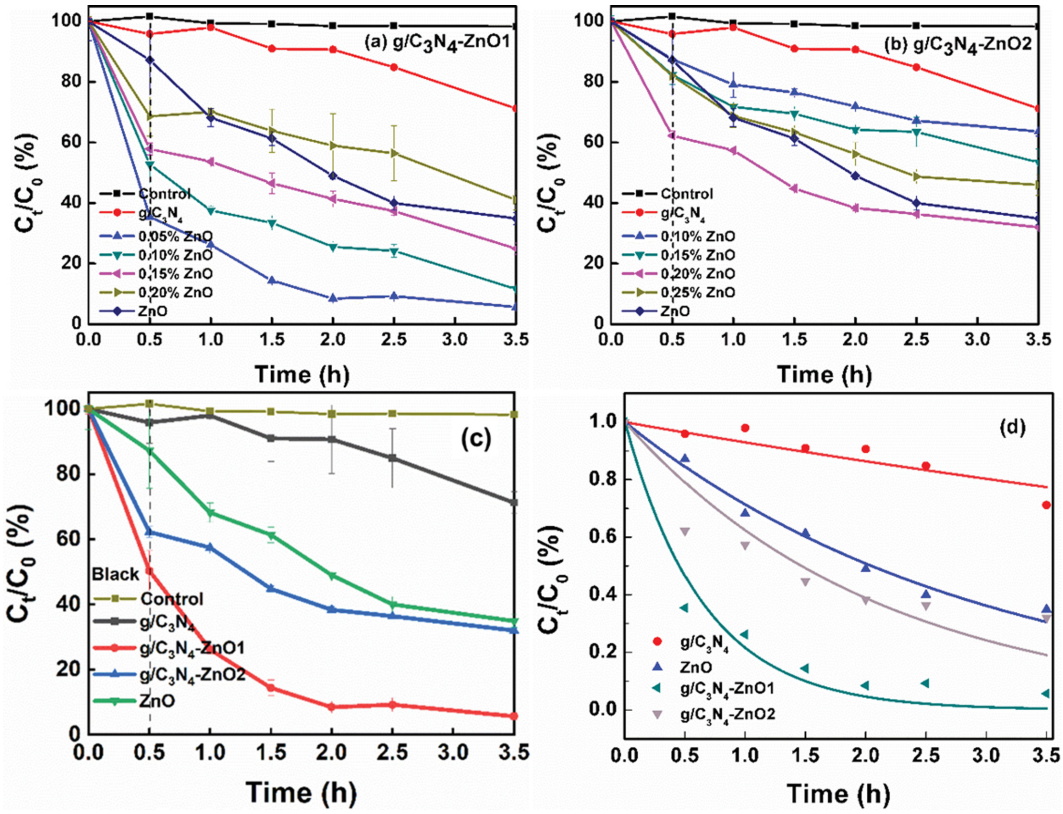


Fig. 4. Concentration decay curves for (a) g/C_3N_4-ZnO1 and (b) g/C_3N_4-ZnO2 with varied ZnO loadings, and (c) a comparison of g/C_3N_4-ZnO1 g/C_3N_4-ZnO2, and (d) the non-linear curve fitting of pseudo-first-order kinetics dataset for g-C_3N_4-ZnO1.

Table 3. The non-linear curve fitting results of the pseudo-first-order kinetics of AMX degradation by g/C_3N_4, ZnO, g/C_3N_4-ZnO1, and g/C_3N_4-ZnO2

Photocatalysts	R^2	k (h^{-1})	$t_{1/2}$ (h)
g/C_3N_4	0.850	0.073	9.495
ZnO	0.986	0.339	2.045
g/C_3N_4-ZnO1	0.962	1.542	0.450
g/C_3N_4-ZnO2	0.842	0.474	1.462

and basic information of AMX is shown in Table S3. After loading of 0.05%-0.15% of ZnO, the degradation capability of g/C_3N_4-ZnO1 is superior to that of control, ZnO, and g/C_3N_4, while 0.20% ZnO deteriorates the photocatalytic ability. For g/C_3N_4-ZnO2, the photoactivity increases when the ZnO loading is in a range of 0.10% to 0.20% but decreases at 0.25%. Only at 0.20%, the photocatalysis ability is better than that of g/C_3N_4. The degradation rate of g/C_3N_4-ZnO1 (0.05% of ZnO) can reach up 95% after 3.5 h, compared to 65% by g/C_3N_4-ZnO2 (0.20% of ZnO). The pseudo-first-order kinetic constant for g/C_3N_4-ZnO1 was estimated to be 1.542 h^{-1}, compared to 0.474 h^{-1} for g/C_3N_4-ZnO2 (Fig. 4(d) and Table 3). These results indicate remarkable structural differences between g/C_3N_4-ZnO1 and g/C_3N_4-ZnO2, resulting from a successive and simultaneous calcination procedure, respectively.

The performance of photocatalytic degradation of AMX and the pseudo-first-order kinetic fitting curves of the photocatalytic degradation process are shown in Fig. 4(d), and the relevant fitting parameters are provided in Table 3. g/C_3N_4-ZnO1 has the best degradation efficiency, and the half-life is 0.805 h, which is 11.33 times higher than g/C_3N_4, 2.52 times higher than ZnO, 3.41 times higher than g/C_3N_4-ZnO2, and performs better than most semiconducting photocatalytic materials (Table S4). The order of degradation efficiency was g/C_3N_4-ZnO1>g/C_3N_4-ZnO2>ZnO>g/C_3N_4 and the order of half-life is g/C_3N_4-ZnO1>ZnO>g/C_3N_4-ZnO2>g/C_3N_4. The results show that g/C_3N_4-ZnO1 preferred the best photocatalytic degradation of AMX, and a synergistic effect between g/C_3N_4 and ZnO was achieved.

The photocatalytic performance was evaluated in five cycles (Fig. 5). For g/C_3N_4-ZnO1, the estimated time for 90% of AMX removal was 2 h at the first cycle, and it slightly delayed to 3.5 h after five cycles. For g/C_3N_4-ZnO2, 3.5 h was needed to degrade 64.0% of AMX at the first cycle, comparing to more than 4 h at the fifth cycle. These results indicate that the reusability of the two catalysts is good.The XRD peaks and FTIR spectra (Fig. S4) of the used samples after five cycles presented very similar patterns as that of pristine ones. There were no observable changes in shapes and positions of both XRD and FTIR peaks in comparison with the pristine ones. These results indicate good structural stability of g/C_3N_4-ZnO1 and g/C_3N_4-ZnO2, and also durable stability of surface functional groups.

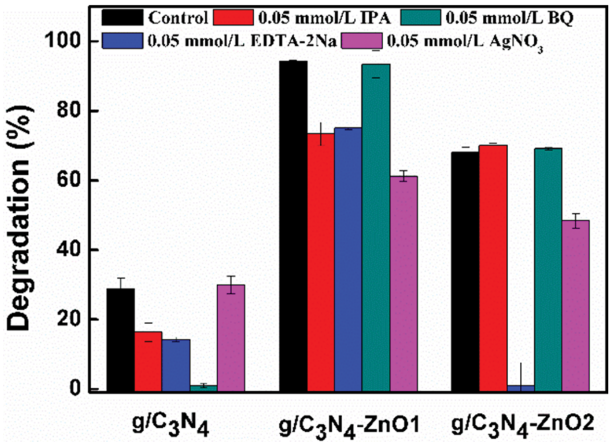


Fig. 6. Active species trapping for AMX with g/C_3N_4, g/C_3N_4-ZnO1 and g/C_3N_4-ZnO2.

4. The Photocatalytic Degradation Mechanism

To determine if adsorption contributes to the photodegradation of AMX, the total organic carbon (TOC) of the solution was measured (Fig. S5). In the initial 0.5 h in the dark no TOC drops were observed for the two catalysts. In the subsequent 3.0 h, there was no TOC change for g/C_3N_4-ZnO1 but a 1.4-14.8% decrease for g/C_3N_4-ZnO2, which was contributed by adsorption and mineralization.

Scavengers were added to probe the generations and the roles of radicals in the photodegradation of AMX (Fig. 6). IPA and EDTA-2Na showed inhibition effects on AMX degradation by g/C_3N_4-ZnO1, while only EDTA-2Na presented distinct effects on g/C_3N_4-ZnO2. The results indicate that both ·OH and h^+ contributed to

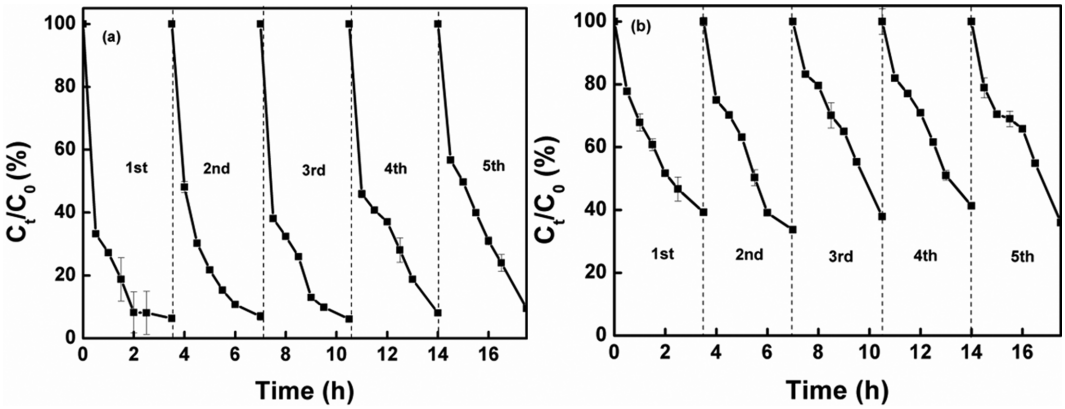


Fig. 5. Recycle and reuse of (a) g/C_3N_4-ZnO1 and (b) g/C_3N_4-ZnO2 under solar light irradiation.

the oxidization in the presence of g/C_3N_4-ZnO1, and there was a strong correlation between ·OH and h^+, while only h^+ dominated the photodegradation of AMX by g/C_3N_4-ZnO2. $\cdot O_2^-$ did not show obvious effects for the two catalysts. Fig. S6 provides the relative quantitative results of $\cdot O_2^-$ quantified by NBT for g/C_3N_4, g/C_3N_4-ZnO1, and g/C_3N_4-ZnO2. For g/C_3N_4, 0.01 mmol/L of $\cdot O_2^-$ was produced at the initial 5 min and kept unchanged till 30 min. It indicates that the yield of $\cdot O_2$ was relatively stable during the photodegrading of AMX. For g/C_3N_4-ZnO1 and g/C_3N_4-ZnO2, $\cdot O_2^-$ occurred in the initial 5 min and gradually decreased to near zero at 30 min. The results are consistent with the radical capture results (Fig. 6). $\cdot O_2^-$ in the g/C_3N_4-ZnO1 and g/C_3N_4-ZnO2 does not affect the photocatalytic degradation of AMX.

The UV-vis diffuse reflectance spectra of the catalysts are provided in Fig. 7(a). g/C_3N_4-ZnO1 and g/C_3N_4-ZnO2 both enhanced the absorption of visible light to a certain extent. The band gaps (E_g) of g/C_3N_4 and ZnO were calculated to be 2.70 eV and 3.14 eV (Fig. 7(b)), respectively, by the Kubelka-Munk equation (Eq. (1)):

$$(\alpha h\nu)^n = A(h\nu - E_g) \quad (1)$$

where α, h, v, E_g, A are the absorption coefficient, Planck constant, light frequency, bandgap energy, and correction coefficient, respectively [23,24]. The constant n in the formula is related to the type of semiconductor electron transfer, which are 1/2 and 2 for g/C_3N_4 and ZnO, since they are an indirect transfer semiconductor and a direct transfer semiconductor, respectively.

The valence band (VB) position of the photocatalyst was measured by X-ray photoelectron spectroscopy (VB XPS), the formula is as follows:

$$E_{NHE} = \Phi + VB_{max} - 4.44 \quad (2)$$

E_{NHE}, Φ and VB_{max} represent the potential of NHE (eV), the electronic work function of the analyzer (4.45 eV) [25], and the maximum value of the valence band determined by the valence band XPS (Fig. 7(c)). The minimum value of CB is obtained by $E_c = E_v - E_g$ [26].

According to the above results of E_g, E_v, and E_C, the band structures of g/C_3N_4 and ZnO are shown in Fig. 7(d), respectively, and the corresponding redox potentials related to the active species are given in the band structure diagram. Based on the results of capture experiments, $\cdot O_2^-$ is the main active species for g/C_3N_4. The generation of $\cdot O_2^-$ follows the reaction $O_2 + e^- \rightarrow \cdot O_2^-$ [27], and its redox potential is −0.33 eV (relative to RHE). The redox potential of $O_2/\cdot O_2^-$ was below CB of g/C_3N_4, so $\cdot O_2^-$ was produced and primarily contributed to the degradation of AMX, in which, ·OH and h^+ also contributed as secondary roles. Under the neutral condition, the redox potential of ·OH/H_2O is 1.965 eV (relative to RHE), which is above 1.980 eV, the valence band (VB) of g/C_3N_4, indicating ·OH can be generated. Due to the relatively small VB value of g/C_3N_4 compared to ·OH/H_2O, the generation of ·OH was limited, it was not the primary active species (Fig. S6).

As revealed above, $\cdot O_2^-$ could occur on g/C_3N_4, but it was not

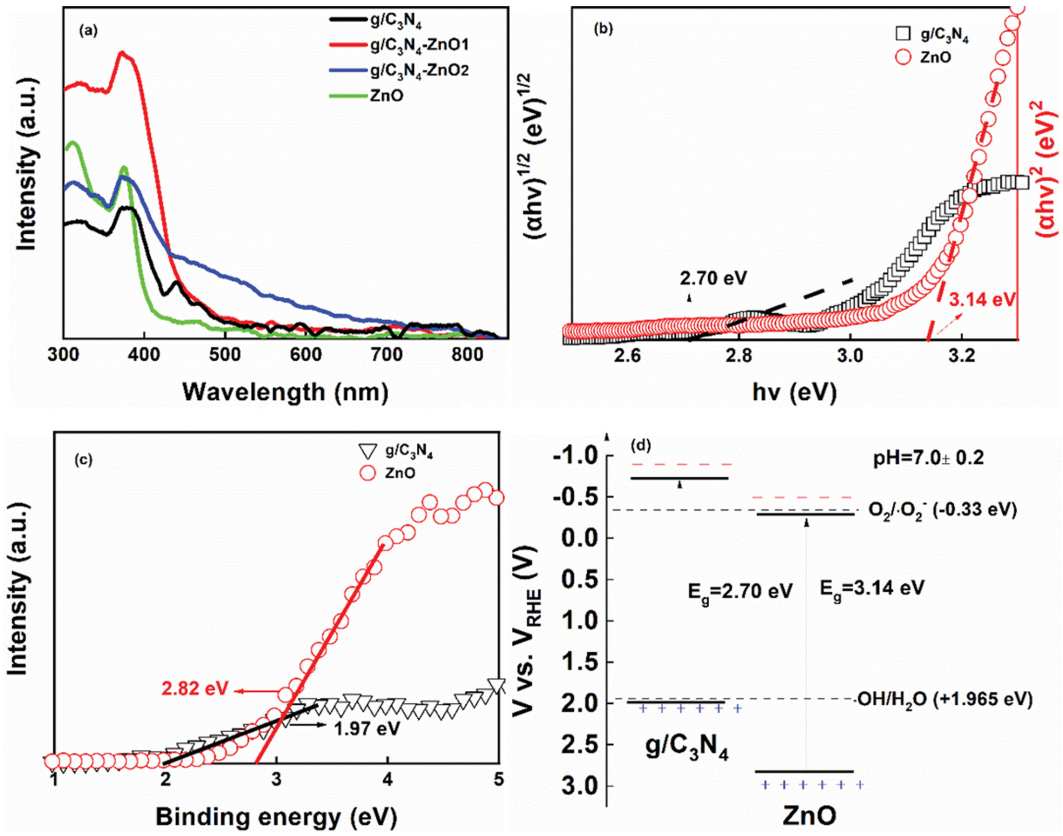


Fig. 7. (a) UV-visible diffuse reflectance spectra of g/C_3N_4, g/C_3N_4-ZnO1, g/C_3N_4-ZnO2 and ZnO, (b) the $(\alpha h\gamma)^{1/2}$ versus $h\gamma$ curves, (c) VBXPS spectra and (d) band structure diagrams of g/C_3N_4 and ZnO.

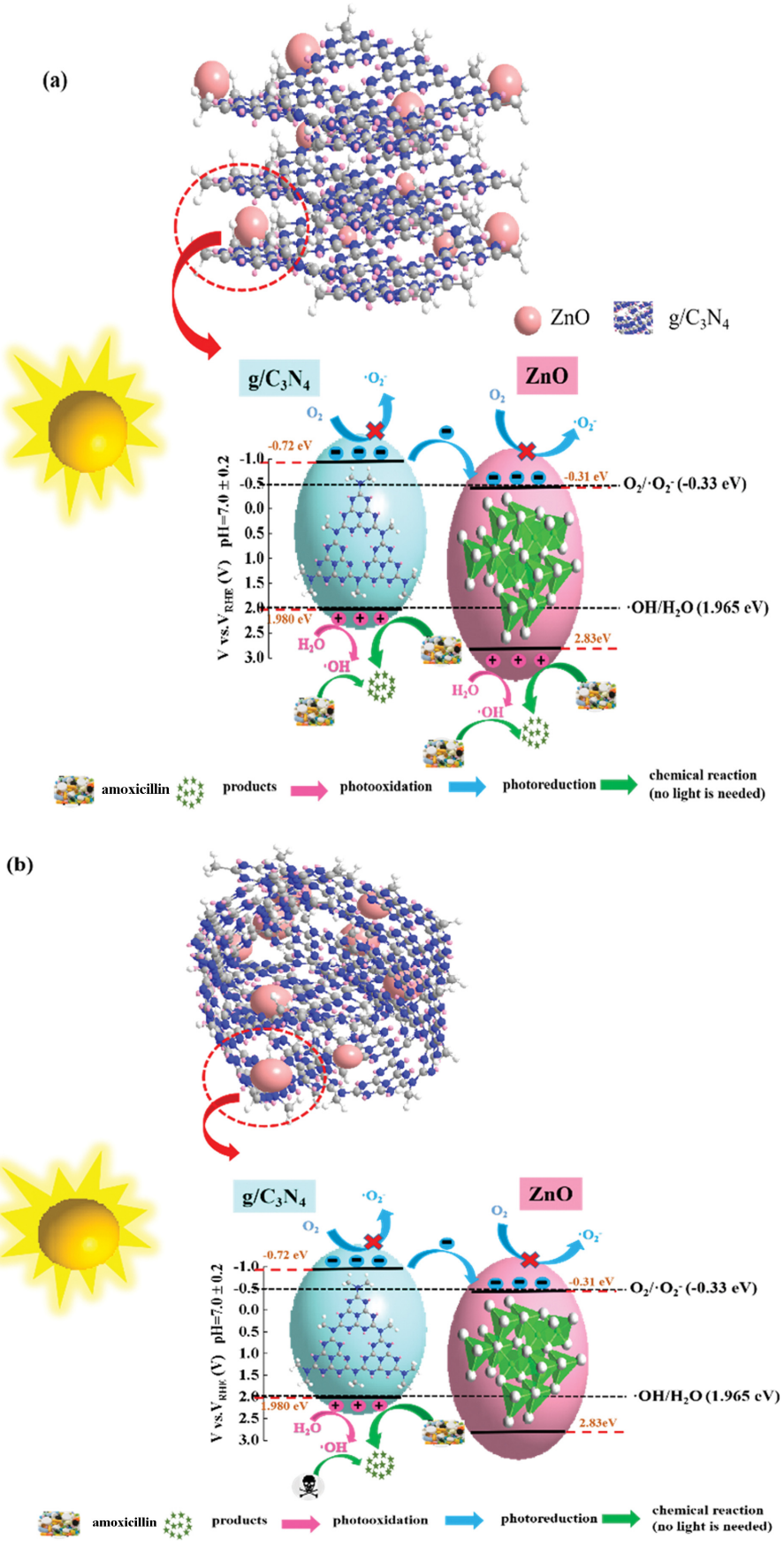


Fig. 8. The mechanism of amoxicillin degradation by (a) g/C_3N_4-ZnO1 and (b) g/C_3N_4-ZnO2.

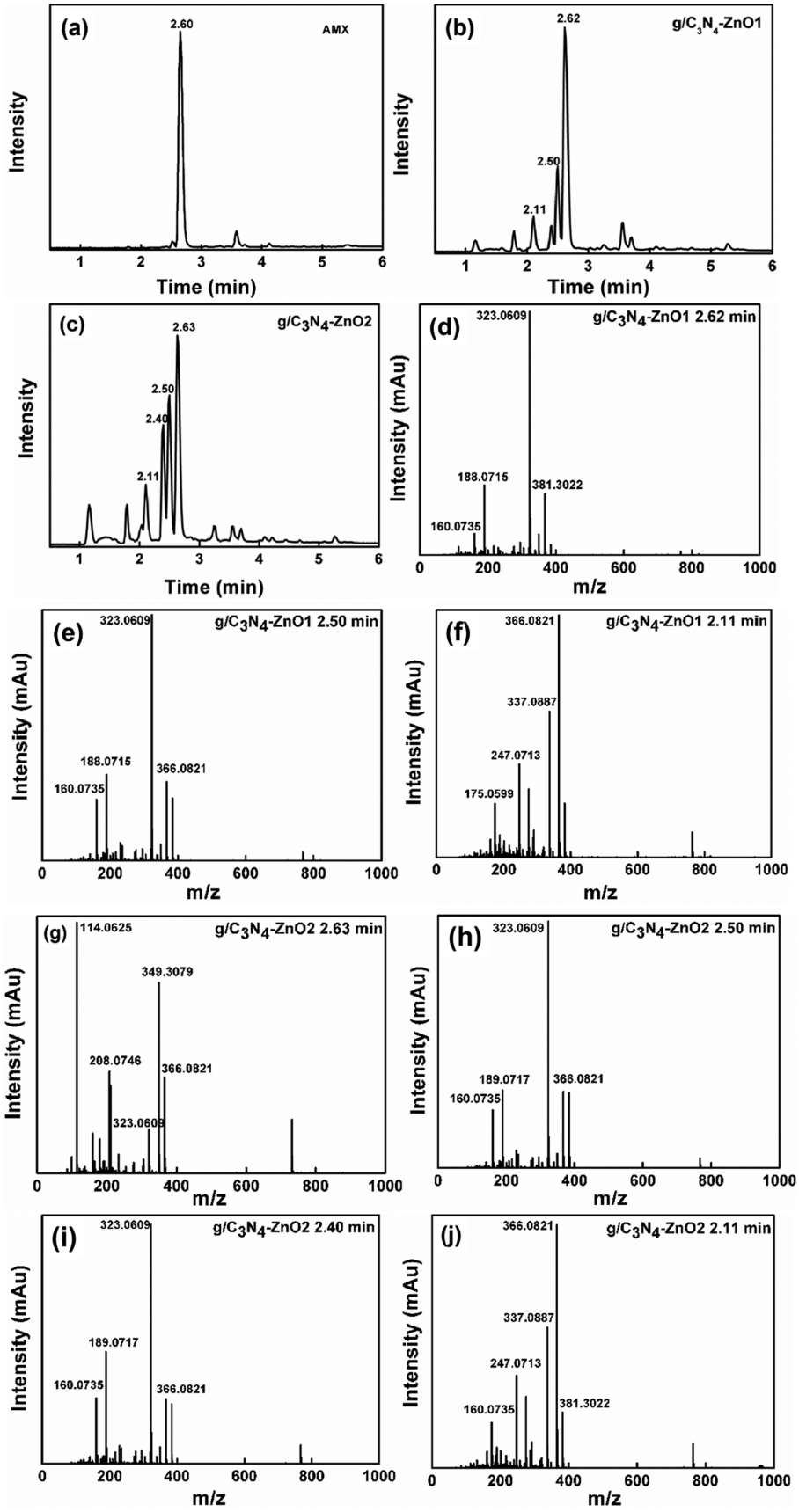


Fig. 9. Total ion flow chromatogram of (a) AMX and transformation products by (b) g/C_3N_4-ZnO1 and (c) g/C_3N_4-ZnO2. Mass spectra at (d) 2.62 min, (e) 2.50 min, (f) 2.11 min by g/C_3N_4-ZnO1, and at (g) 2.63 min, (h) 2.5 min, (i) 2.4 min and (j) 2.11 min by g/C_3N_4-ZnO2.

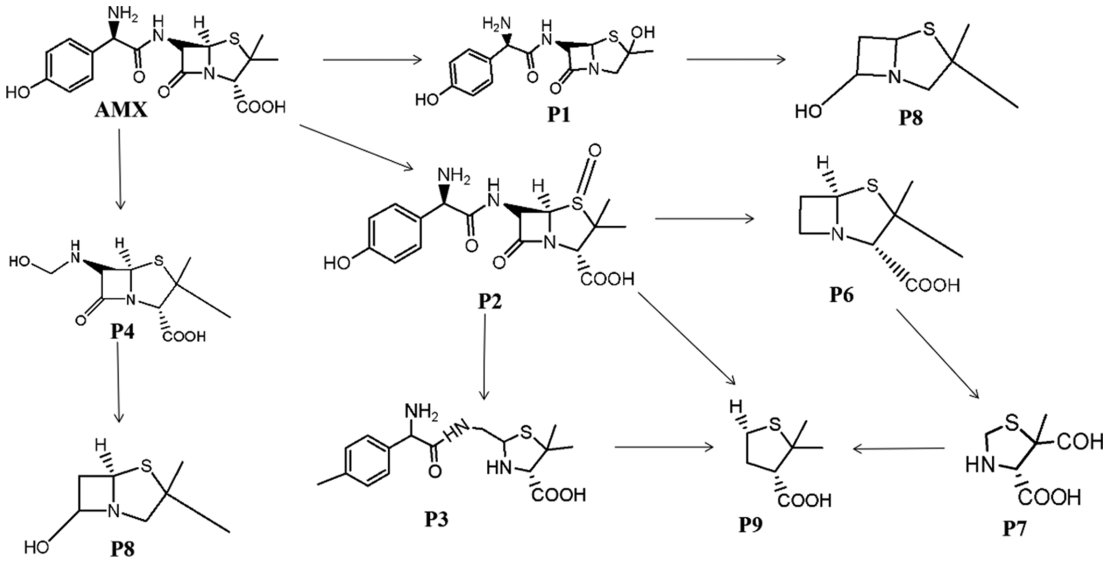


Fig. 10. The proposed pathway for AMX photodegradation by g/C_3N_4-ZnO1.

observed for both g/C_3N_4-ZnO1 and g/C_3N_4-ZnO2. That means electrons from CBs of the two catalysts transferred to the surface of ZnO in the composites. The CB (−0.31 eV, relative to RHE) of ZnO is below the redox potential (−0.33 eV, relative to RHE) of $O_2/\cdot O_2^-$, so the electrons which have transferred to CB of ZnO cannot react with O_2 to produce $\cdot O_2^-$. For g/C_3N_4-ZnO1, ·OH and h^+ are the main active substances. According to Fig. 7(d), when the pH is about 7.0, the VB of ZnO is +2.830 eV, which is higher than the redox potential of OH/H_2O (+1.965 eV), leading to the production of ·OH through the reaction of $H_2O+h^+\rightarrow\cdot OH$. h^+ from VB of ZnO was not transferred to that of g/C_3N_4. If this had happened, the production of ·OH would be very limited since the VB (1.980 eV) of g/C_3N_4 is only slightly higher than the redox potential of OH/H_2O (+1.965 eV). The contribution of ·OH to AXM photodegradation was not significant. This is not consistent with the radical capture results; therefore, h^+ in ZnO was not transferred. For g/C_3N_4-ZnO2, the main active species is h^+. ·OH and $\cdot O_2^-$ have little effect on the degradation of AMX. It was inferred that ZnO was wrapped by g/C_3N_4. Under visible light irradiation, ZnO, which was surrounded, hardly absorbs enough photons and most of the photons are absorbed by g/C_3N_4. The electrons in the valence band cannot jump into the CB of ZnO. There is no photogenerated hole-electron pair generated. ·OH cannot be produced in the VB of ZnO, but it can accept the electrons migrated from CB of g/C_3N_4. Thus, electrons from CB of g/C_3N_4 cannot react with O_2 to produce $\cdot O_2^-$. Therefore, in the g/C_3N_4-ZnO2 system, only holes in the g/C_3N_4 valence band participate in the degradation of AMX. The synergistic mechanisms for the heterostructured binary photocatalyst are illustrated in Fig. 8. The difference in photocatalytic mechanism between the two catalysts is from their structures resulting from a successive and simultaneous calcination procedure.

5. Degradation Products and Pathway

Three retention peaks at 2.62 min, 2.50 min, and 2.11 min were observed in the UPLC spectrum for g/C_3N_4-ZnO1 after 1.0 h, and four retention peaks at 2.63 min, 2.50 min, 2.40 min, and 2.11 min for g/C_3N_4-ZnO2 after 1.5 h (Figs. 9(a)-(c)).Their corresponding mass spectra are provided in Figs. 9(d)-(j). Twelve intermediate degradation products (P1-P12) were revealed (Table S5). Similar hydrolytic pathways were suggested for the two catalysts, and two primary degradation steps were inferred (Fig. 10 and Fig. S7). The first is a hydroxylation process [28]. A hydroxyl group was added to AMX to produce intermediates P1, P4, P8, and P11. The lactam plus thiazolidine ring was intact during hydroxylation [29]. Therefore, the attack of hydroxyl radical was expected to occur in a position where the AMX molecule was more vulnerable to electrophilic attack, for example, the lone pair of electrons in nitrogen atoms. Another degradation pathway is the opening of the four-membered β-lactam ring and producing a series of derivatives without a β-lactam ring, such as P3, P9, P7, P10, P11, and P12. P3 was reported as a hydrolysate of AMX or the opening of the β-lactam ring in P1 and P2 [30,31]. The production of intermediate P7 proved the oxidation of methyl in the thiazolidine ring. P4 proved the bond breaking between amino nitrogen and carbonyl nitrogen [32]. The antibacterial potential mainly originated from the binding of the β-lactam ring with penicillin-binding proteins (PBPs) [33,34]. After opening the lactam ring, the antibacterial potential was expected to drop dramatically.

The toxicity of AMX (m/z 365.0821) and its photocatalytic intermediates by the two catalysts was assessed using the ECOSAR program. The results are provided in Table 4. AMX itself is classified as "harmful" (10-100 mg/L) since it could cause acute toxicity to daphnids and shows effectiveness to green algae and is "toxic" when considering its chronic effect on daphnid. The intermediates P6 (m/z 187.0715) and P8 (m/z 187.0715) are "acute harmful" to daphnid, while they are "toxic" to daphnid in a view of the chronic effect. And P6 (m/z 187.0715) is also "harmful" to algae. In addition, P1 (m/z 322.0609) and P10 (m/z 207.0746) are "chronic harmful" to daphnid. Except for these intermediates mentioned above, the others are non-harmful and they will not cause acute or chronic toxicity to both daphnia and green algae. The result was comput-

Table 4. The ECOSAR (ecological structure-activity relationship) prediction on AMX and its transformation products

Transformation products	Daphnid		Green algae	ECOSAR class
	$LC_{50,48\,hr}$ (ppm)	ChV (ppm)	$EC_{50,96\,hr}$ (ppm)	
AMX	15.3	3.19	30.3	Phenol amines
m/z 187.0715	33.8	2.35	39.2	Aliphatic amines
m/z 159.0735	97.0	6.11	137	Aliphatic amines
m/z 322.0609	495*	28.9*	816*	Aliphatic amines
m/z 207.0746	259	15.4	413	Aliphatic amines
m/z 380.3022	2,450*	153*	3,490*	Aliphatic amines
m/z 174.0599	26,300	1,280	63,100	Aliphatic amines
m/z 336.0887	2,850*	175*	4,260*	Aliphatic amines
m/z 246.0713	1,610	101	2,310	Aliphatic amines
m/z 159.0735	1,020	95.8	718	Neutral organics

Note: *=asterisk designate: chemical may not be soluble enough to measure this predicted effect. If the effect level exceeds the water solubility by 10x, typically no effects at saturation (NES) are reported.
$LC_{50,48\,hr}$: 48-h Half Lethal Concentration; $EC_{50,96\,hr}$: 96-h concentration for 50% of maximal effect; ChV: Chronic Value.
Yellow boxes, toxic: 1 ppm<LC_{50}/EC_{50}/ChV<10 ppm; blue boxes, harmful: 10 ppm<LC_{50}/EC_{50}/ChV<100 ppm; green boxes, not harmful: LC_{50}/EC_{50}/ChV>100 ppm.

erized based on structure-activity relationships for each intermediate, and their overall toxicity to specific creature needs to be assessed by considering the exposure concentration and contact time in the future.

CONCLUSIONS

Two g/C_3N_4-ZnO composite photocatalysts, g/C_3N_4-ZnO1 and g/C_3N_4-ZnO2, were successfully synthesized through a successive and simultaneous calcination procedure, respectively. Heterojunctions formed between the two components, which were effective to promote the efficient separation of photogenerated carriers, and then enhanced the degradation of 100 mg/L of AMX. The degradation rate of g/C_3N_4-ZnO1 was 1.54 times that of g/C_3N_4-ZnO2 and was 11.33 and 2.52 times compared with g/C_3N_4 and ZnO, respectively, at a 3.5-h reaction period, with an initial AMX concentration of 100 mg/L, dosage of 0.3 g/L, and solution pH at 7.0± 0.2. The degradation performance was excellent even after five cycles and 90.5% of AMX was mitigated. Adsorption did not significantly contribute to AMX degradation by g/C_3N_4-ZnO1 and less than 14.8% of AMX was mineralized by g/C_3N_4-ZnO2. For g/C_3N_4-ZnO1, electrons migrated from the conduction band of g/C_3N_4 to the conduction band of ZnO *via* the heterojunction. ·OH and h^+ were the main active species responsible for AMX degradation, compared to $\cdot O_2^-$ dominated for g/C_3N_4. Twelve intermediate products were identified, and two degradation pathways were inferred for g/C_3N_4-ZnO1 and g/C_3N_4-ZnO2, respectively. Finally, products without the lactam ring were achieved, which were inactive to bind with penicillin-binding proteins (PBPs) and lost most of the antibacterial potencies, and the ecotoxicity was also dramatically decreased as revealed by the ECOSAR predictions.

ACKNOWLEDGEMENTS

This work was supported by the National Natural Science Foundation of China (51978052) and Beijing Municipal Education Commission through the Innovative Transdisciplinary Program "Ecological Restoration Engineering (No. GJJXK210102)".

SUPPORTING INFORMATION

Additional information as noted in the text. This information is available via the Internet at http://www.springer.com/chemistry/journal/11814.

REFERENCES

1. A. Timm, E. Borowska, M. Majewsky, S. Merel, C. Zwiener, S. Bräse and H. Horn, *Sci. Total Environ.*, **651**, 1605 (2019).
2. L. Yao, Y. Wang, L. Tong, Y. Deng, Y. Li, Y. Gan, W. Guo, C. Dong, Y. Duan and K. Zhao, *Ecotoxicol. Environ. Saf.*, **135**, 236 (2017).
3. W. Chen, J. Shen, Z. Wang, X. Liu, Y. Xu, H. Zhao and D. Astruc, *Chem. Sci.*, **12**(35), 11722 (2021).
4. N. Taoufik, W. Boumya, M. Achak, M. Sillanpää and N. Barka, *J. Environ. Manage.*, **288**, 112404 (2021).
5. B. Wei, C. Niu, G. Zhou, J. Sun, Q. Mei, Z. An, M. Li and M. He, *Appl. Surf. Sci.*, **391**, 72 (2017).
6. D. Zhu and Q. Zhou, *Appl. Catal. B*, **282**, 119574 (2021).
7. N. Ghane, S. K. Sadrnezhaad and S. M. Hosseini H., *Appl. Surf. Sci.*, **534**, 147563 (2020).
8. C. B. Ong, L. Y. Ng and A. W. Mohammad, *Renewable Sustainable Energy Rev.*, **81**, 536 (2018).
9. N. Li, Y. Tian, J. Zhao, J. Zhang, W. Zuo, L. Kong and H. Cui, *Chem. Eng. J.*, **352**, 412 (2018).
10. Y. Liu, H. Liu, H. Zhou, T. Li and L. Zhang, *Appl. Surf. Sci.*, **466**, 133 (2019).
11. D. Shen, X. Li, C. Ma, Y. Zhou, L. Sun, S. Yin, P. Huo and H. Wang, *New J. Chem.*, **44**(38), 16390 (2020).
12. W. Li, D. Li, J. Wang, Y. Shao, J. You and F. Teng, *J. Mol. Catal. A: Chem.*, **380**, 10 (2013).

13. H. Yu, J. Huang, L. Jiang, Y. Shi, K. Yi, W. Zhang, J. Zhang, H. Chen and X. Yuan, *Chem. Eng. J.*, **402**, 126187 (2020).
14. E.-P. Bao, R. Dong, S. Zhang, H. Li, W. Zhang, J. Zou and Q. Xu, *Catal. Lett.*, **151**(12), 3437 (2021).
15. X. Yuan, S. Qu, X. Huang, X. Xue, C. Yuan, S. Wang, L. Wei and P. Cai, *Chem. Eng. J.*, **416**, 129148 (2021).
16. N. Kumaresan, M. M. A. Sinthiya, M. Praveen Kumar, S. Ravichandra and R. Ramesh Babu, *Arabian J. Chem.*, **13**, 2826 (2020).
17. F. He, B. Zhu., B. Cheng, J. Yu, W. Ho and W. Macyk, *Appl. Catal. B*, **272**, 119006 (2020).
18. Z. Li, N. Xiong and G. Gu, *Dalton Trans.*, **48**(1), 182 (2018).
19. C. A. Jaramillo-Páez, J. A. Navío, M. C. Hidalgo and M. Macías, *Catal. Today*, **313**, 12 (2018).
20. C. Zhang, M. Jia, Z. Xu, W. Xiong, Z. Yang, J. Cao, H. Peng, H. Xu, Y. Xiang and Y. Jing, *Chem. Eng. J.*, **430**, 132652 (2022).
21. B. Liu, C. Bie, Y. Zhang, L. Wang, Y. Li and J. Yu, *Langmuir*, **37**(48), 14114 (2021).
22. L. Shi, F. Wang, Y. Wang, D. Wang, B. Zhao, L. Zhang, D. Zhao and D. Shen, *Sci. Rep.*, **6**(1), 21135 (2016).
23. J. Wen, J. Xie, X. Chen and X. Li, *Appl. Surf. Sci.*, **391**, 72 (2017).
24. J. Qu, Y. Du, Y. Feng, J. Wang, B. He, M. Du, Y. Liu and N. Jiang, *Mater. Sci. Semicond. Process*, **112**, 105023 (2020).
25. K. N. Van, H. T. Huu, V. N. Nguyen Thi, T. L. Le Thi, D. H. Truong, T. T. Truong, N. N. Dao, V. Vo, D. L. Tran and Y. Vasseghian, *Chemosphere*, **289**, 133120 (2022).
26. Y. Nosaka, M. Nishikawa and A. Y. Nosaka, *Molecules*, **19**(11), 18248 (2014).
27. Z. Diao, J. Jin, M. Zou, H. Liu, J. Qin, X. Zhou, W. Qia, P. Guo, L. Kong and W. Chu, *Sep. Purif. Technol.*, **278**, 119620 (2021).
28. A. G. Trovó, R. F. Pupo Nogueir, A. Agüera, A. R. Fernandez-Alba and S. Malato, *Water Res.*, **45**(3), 1394 (2011).
29. Y. Zhang, Y. Xu, Y. Zhang and L. Teik Thye, *Chem. Eng. J.*, **372**, 420 (2019).
30. I. Gozlan, A. Rotstei and D. Avisa, *Chemosphere*, **91**(7), 985 (2013).
31. X. Zhang, Y. Guo, Y. Pan and X. Yang, *Sci. Ecotechnol.*, **3**, 100051 (2020).
32. H. Zeng, H. Zhan, L. Deng and Z. Shi, *J. Water Process. Eng.*, **33**, 101084 (2020).
33. B. Wei, C. Niu, G. Zhou, J. Sun, Q. Mei, Z. An, M. Li and M. He, *Environ. Res.*, **207**, 112623 (2022).
34. P. Chen, F. Wang, Z.-F. Chen, Q. Zhang, Y. Su, L. Shen, K. Yao, Y. Liu, Z. Ca, W. Lv and G. Liu, *Appl. Catal. B*, **204**, 250 (2017).

Supporting Information

Construction of g/C_3N_4-ZnO composites with enhanced visible-light photocatalytic activity for degradation of amoxicillin

Shuhan Sun*, Shiling Li*, Yibing Hao*, Xiao Yang, and Xiaomin Dou*,***,†**

*Beijing Key Lab for Source Control Technology of Water Pollution, College of Environmental Science and Engineering, Beijing Forestry University, Beijing 100083, China
**Key Laboratory of Land Surface Pattern and Simulation, Institute of Geographic Sciences and Natural Resources Research, Chinese Academy of Sciences, Beijing 100101, China
***Engineering Research Center for Water Pollution Source Control & Eco-remediation, Beijing Forestry University, Beijing 100083, China
(*Received 15 March 2022 • Revised 14 May 2022 • Accepted 18 May 2022*)

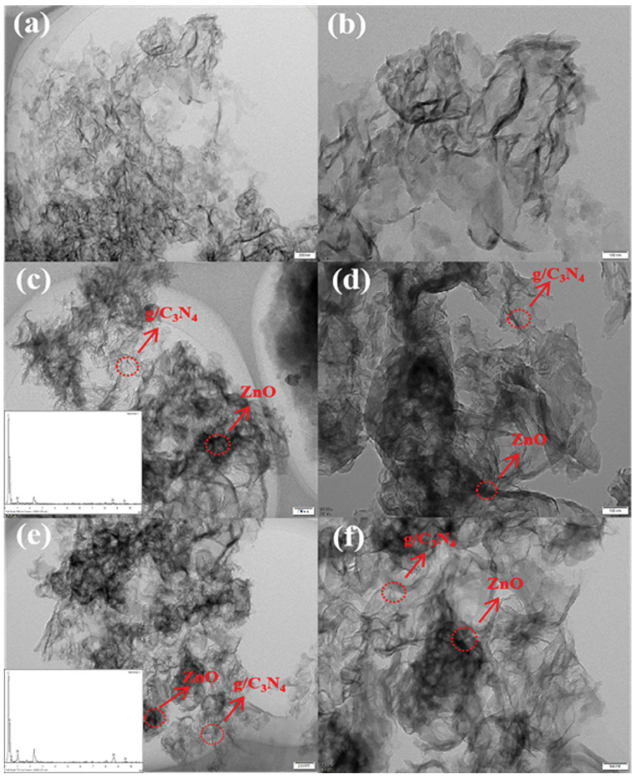


Fig. S1. TEM images of (a)-(b) g/C_3N_4, (c)-(d) g/C_3N_4-ZnO1 and (e)-(f) g/C_3N_4-ZnO2 and EDX mapping of g/C_3N_4-ZnO1 (Spectrum 1) and g/C_3N_4-ZnO2 (Spectrum 2).

Table S1. The C, N and Zn contents (at%) of g/C_3N_4, g/C_3N_4-ZnO1, g/C_3N_4-ZnO2 and ZnO based on XPS results

	Photocatalysts	g/C_3N_4	g/C_3N_4-ZnO1	g/C_3N_4-ZnO2	ZnO
C1s	C=C (284.7 eV)	4.71%	3.18%	1.81%	0
	N=C-N (288.0 eV)	88.80%	90.86%	91.93%	0
	π excitation (293.7 eV)	6.49%	5.94%	6.25%	0
N1s	C=N-C /N-Zn (398.4 eV)	72.44%	65.53%	55.82%	0
Zn2p	Zn $2p_{3/2}$ (1,021.9 eV)	0	62.40%	71.97%	59.31%
	Zn $2p_{5/2}$ (1,045.1 eV)	0	37.60%	28.03%	40.69%

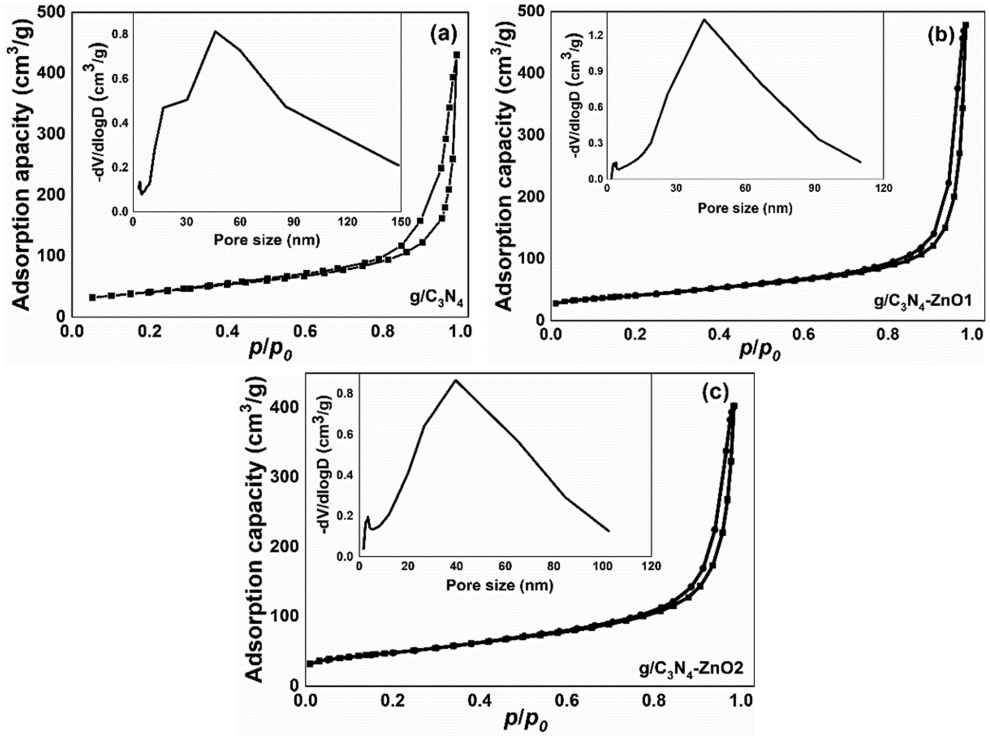


Fig. S2. BET and pore size distributions of (a) g/C_3N_4, (b) g/C_3N_4-ZnO1 and (c) g/C_3N_4-ZnO2.

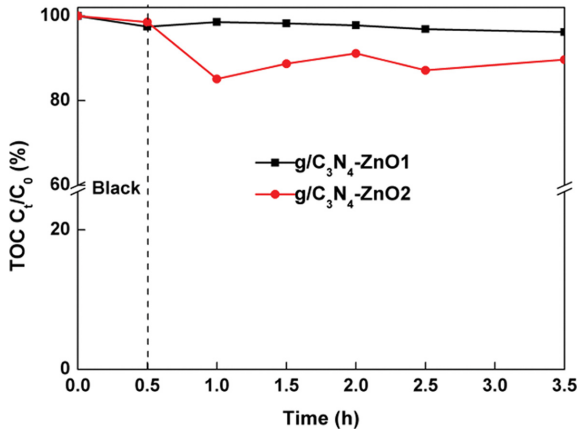


Fig. S3. The changes of total organic carbon (TOC) in solutions by g/C_3N_4-ZnO1 and g/C_3N_4-ZnO2.

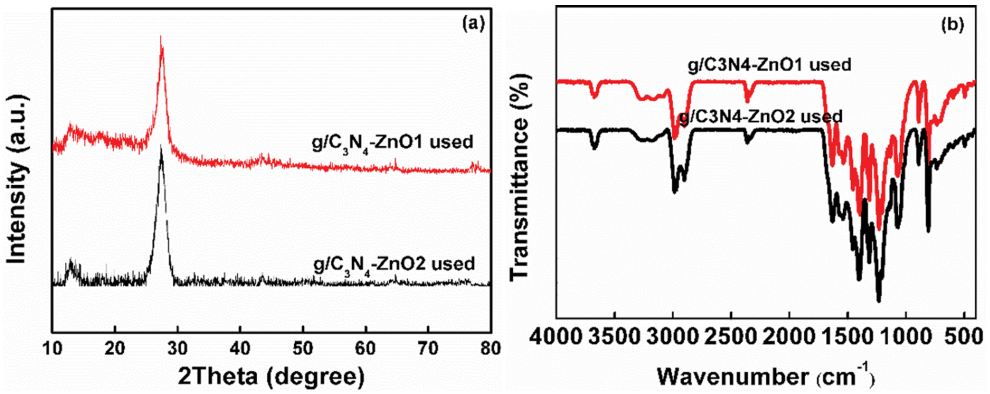


Fig. S4. (a) XRD and (b) FTIR spectra of g/C_3N_4-ZnO1, g/C_3N_4-ZnO2 before and after reaction.

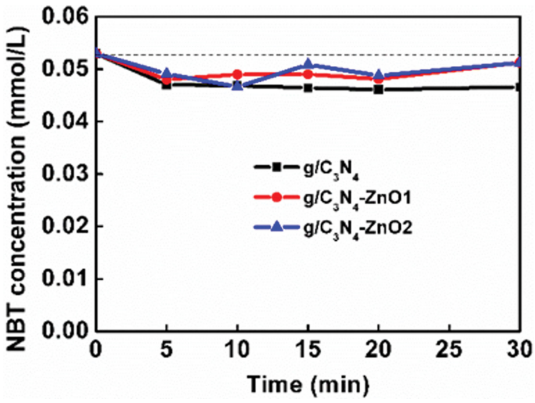


Fig. S5. The relatively quantitative analyses of the dominant active species of $\cdot O_2^-$ based on the NBT transformation by g/C_3N_4, g/C_3N_4-ZnO1 and g/C_3N_4-ZnO2.

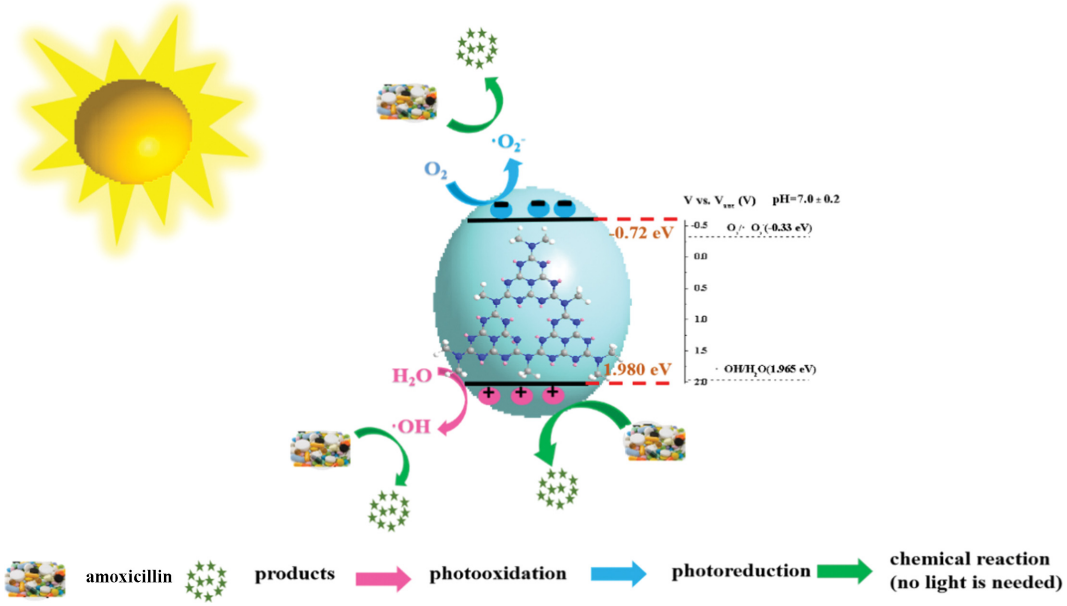
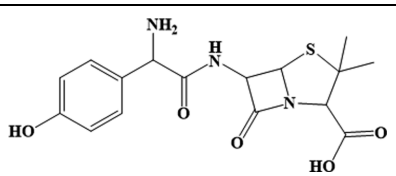


Fig. S6. Demonstration of the mechanism of amoxicillin degradation by g/C_3N_4.

Table S2. The contents of C, N, O, Zn in g/C_3N_4, g/C_3N_4-ZnO1, g/C_3N_4-ZnO2 and ZnO

Photocatalysts	C (%)	N (%)	O (%)	Zn (%)
g/C_3N_4	42.97	56.07	0.95	0
g/C_3N_4-ZnO1	41.70	56.82	1.13	0.35
g/C_3N_4-ZnO2	40.37	57.14	1.99	0.49
ZnO	0	0	49.65	50.35

Table S3. The structure of amoxicillin

Name	Chemical formula	Structural formula	Relative molecular mass	CAS
Amoxicillin	$C_{16}H_{19}N_3O_5S$		365.404	26787-78-0

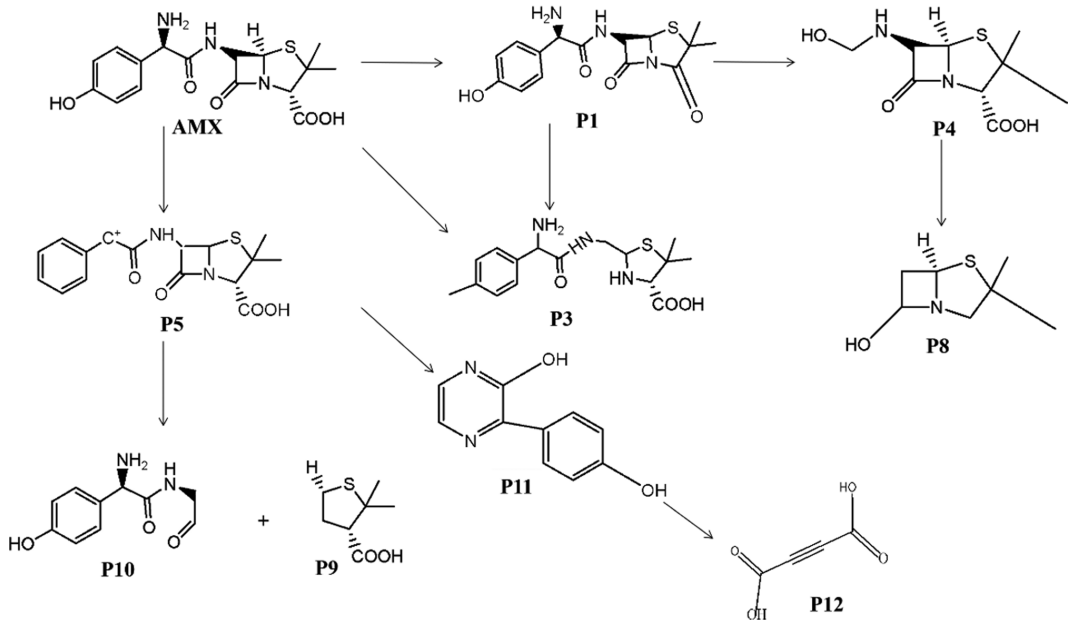


Fig. S7. The proposed pathway of AMX photodegradation by g/C_3N_4-ZnO2.

Table S4. The comparison of amoxicillin degradation by different kinds of photocatalysts

Photocatalysts	Initial concentration (mg/L)	Dosage (g/L)	light source (W)	pH	Time	Efficiency (%)	Reference
g/C_3N_4-ZnO	20	0.3	vis	7	3.5	95	This study
(g-C_3N_4)-Ag-TiO_2	20		UV-vis		6 h	80	[1]
1Pt-5Bi-TiO_2	10	0.5	vis	11	2 h	87.67	[2]
3.0 wt%Ag-TiO_2	20	4	vis		5 h	51.5	[3]
C_3N_4-$MnFe_2O_4$-graphene	20	1	vis		90 min	70	[4]
Fe,N-Co-doped TiO_2	30	1	vis	3.5	5 h	58.61	[5]
G-$BiOBr_{0.2}I_{0.8}$	20		vis		5 h	93.2	[6]
g-C_3N_4-20@Ni–Ti LDH NCs	100	1.25	vis		150 min	83	[7]
Hetero-junction p-CuO/n-ZnO	50	0.5	vis	11	4 h	93.02	[8]

Table S5. The transformation products of AMX by g/C_3N_4-ZnO1 and g/C_3N_4-ZnO2 revealed by MS spectra

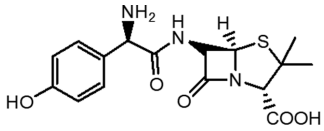
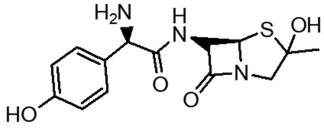
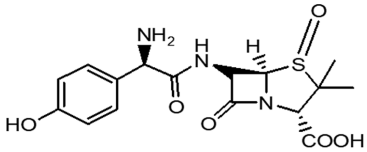
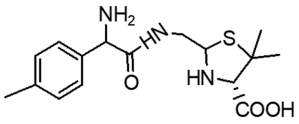
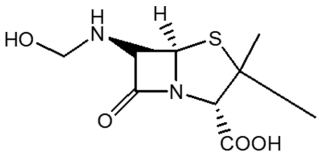
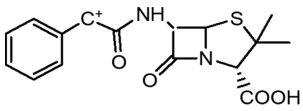
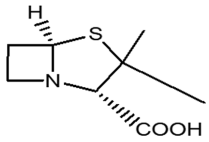
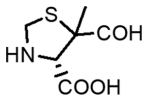
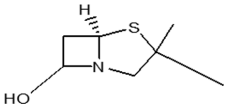
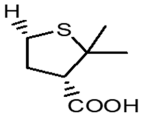
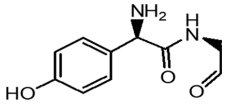
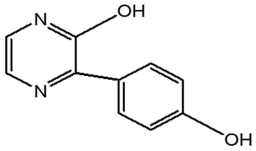
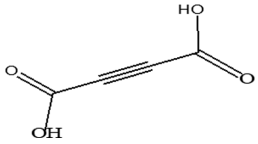
Sample	Molecular formula	Structure	Fragments (m/z)
AMX	$C_{16}H_{19}N_3O_5S$		365.0821
P1	$C_{14}H_{17}N3O_4S$		322.0609
P2	$C_{16}H_{19}N_3O_6S$		380.3022

Table S5. Continued

Sample	Molecular formula	Structure	Fragments (m/z)
P3	$C_{16}H_{23}N_3O_3S$		336.0887
P4	$C_9H_{14}N_2O_4S$		246.0713
P5	$C_{17}H_{20}N_2O_4S$		348.3079
P6	$C_8H_{13}NO_2S$		187.0715
P7	$C_6H_9NO_3S$		174.0599
P8	$C_7H_{13}NOS$		159.0735
P9	$C_7H_{12}O_2S$		160.0611
P10	$C_{10}H_{12}N_2O_3$		207.0746
P11	$C_{10}H_8N_2O_2$		188.0717
P12	$C_4H_2O_4$		113.0625

REFERENCES

1. K. H. Leong, S. L. Liu, L. C. Sim, P. Saravanan, M. Jang and S. Ibrahim, *Appl. Surf. Sci.*, **358**, 370 (2015).
2. M. Salimi, M. Behbahani, H. R. Sobhi, M. Gholami, A. Jonidi Jafari, R. Rezaei Kalantary, M. Farzadkia and A. Esrafili, *New J. Chem.*, **43**(3), 1562 (2019).
3. K. H. Leong, B. L. Gan, S. Ibrahim and P. Saravanan, *Appl. Surf. Sci.*, **319**, 128 (2014).
4. X. Wang, A. Wang and J. Ma, *J. Hazard. Mater.*, **336**, 81 (2017).
5. C. G. Aba-Guevara, I. E. Medina-Ramírez, A. Hernández-Ramírez, J. Jáuregui-Rincón, J. A. Lozano-Álvarez and J. L. Rodríguez-López, *Ceram. Int.*, **43**(6), 5068 (2017).
6. M. Yadav, S. Garg, A. Chandra and K. Hernadi, *J. Colloid Interface Sci.*, **555**, 304 (2019).
7. R. Abazari, A. R. Mahjoub, S. Sanati, Z. Rezvani, Z. Hou and H. Dai, *Inorg. Chem.*, **58**(3), 1834 (2019).
8. Y. Belaissa, D. Nibou, A. A. Assadi, B. Bellal and M. Trari, *J. Taiwan Inst. Chem. Eng.*, **68**, 254 (2016).